PHYSICAL REVIEW LETTERS **128,** 058001 (2022)

Ripple Patterns Spontaneously Emerge through Sequential Wrinkling Interference in Polymer Bilayers

Luca Pellegrino, Annabelle Tan, and João T. Cabral*
Department of Chemical Engineering, Imperial College London, London SW7 2AZ, United Kingdom

(Received 24 September 2021; accepted 10 January 2022; published 2 February 2022)

We report the formation of "ripple" patterns by the sequential superposition of nonorthogonal surface waves excited by the spontaneous buckling of polymeric bilayers. Albeit of a different nature and micron scale compared to the familiar sedimentary ripples caused by gentle wave oscillations, we find commonalities in their topography, defects, and bifurcations. The patterns are rationalized in terms of a defect density that depends on the relative angle between generations, and a constant in-plane bending angle that depends on skin thickness. A minimal wave summation model enables the design of ripple and checkerboard surfaces by tuning material properties and fabrication process.

DOI: 10.1103/PhysRevLett.128.058001

The coupling between fluid motion, both unidirectional and periodic, and sediment transport, gives rise to the familiar yet fascinating, self-organization processes [1,2] responsible for the formation of "ripples" in sand beds and beach dunes. Flows of different orientation induced two-dimensional instabilities [3–5] with in-plane secondary length scales. These transverse interference morphologies can be described in terms of the Benjamin-Feir instability, associated to the loss of stability of travelling waves to sideband perturbations [6,7], and are reminiscent of two-dimensional patterns induced by a Rayleigh-Taylor instability in stratified thin layers of different density [8]. Analogous patterns are found in folded, layered rock formations, developing a range of orthogonal to non-orthogonal interference patterns [9–11].

Striking periodic and aperiodic structures also emerge in biological morphogenesis [12], for instance in the epicuticular topography of certain insect wings, such as dragonflies or cicadae [13], modulating appearance and function, such as structural color and superhydrophobicity.

Buckling instabilities in bi- and multilayered soft materials [14,15] provide a facile and effective means for periodic pattern formation over large areas down to the nanoscale. Spontaneous wrinkling occurs when a bilayer comprising a stiff film atop a soft substrate is compressed beyond a critical limit [16], applied via mechanical strain [17], temperature cycling [18] or solvent-induced swelling, and evaporation [19,20]. An efficient way to form bilayer structure employs plasma oxidation (or UV ozonolysis) [21] of an elastomeric material, such as polydimethylsiloxane (PDMS), proceeding via the frontal oxidation and growth of a $\simeq 10$ nm glassy skin [22,23]. Prescribed topographies are readily excited and tuned by the applied strain field, skin thickness, and modulus, and multiaxial strains give rise to a plethora of complex patterns including dimples, herringbones (chevrons), checkerboards, or labyrinthine features which result in a wrinkling mode selection determined by an overall elastic and bending energy minimization [24,25]. Although not a dominant mode, extensive checkerboard or "spiky" topographies can be induced by first generating a one-dimensional wrinkled surface, which is then replicated and wrinkled again along the orthogonal direction [26,27], with individually set amplitudes and wavelengths [28].

With these ideas in mind, we explore wrinkling wave superposition as a means to designing surface patterns, and examine the capabilities and limitations of this concept. Specifically, we consider the sequential juxtaposition of two wrinkling generations induced by uniaxial strain of a bilayer, but with a variable angle between them. Nontrivial aspects of this methodology include the fact that the second wrinkling event no longer takes place onto a planar bilayer, and coupling with the first generation topography is expected. The experimental realization of such wave superposition is relatively straightforward, as shown in Fig. 1(a). A PDMS (Sylgard 184, Dow Corning) slab is clamped in a motorized linear strain stage [Fig. 1(b)], uniaxially stretched and then subjected to oxygen plasma oxidation (Diener Femto 40 kHz, 20 W, 1 mbar), forming a glassy skin of thickness, h_1, and modulus, E_{f1}. Upon strain release, the first wrinkling generation is formed, with prescribed wavelength, $\lambda_{\parallel}$, and amplitude, $A_{\parallel}$. Interference is achieved by superposing the second wrinkling generation at a prescribed angle, $0° \leq \theta \leq 90°$, termed "compression angle." The $1D_{\parallel}$ coupon is first replicated into fresh PDMS, to remove the fragile oxide layer and residual stresses, while preserving the sinusoidal topography. The replica is tilted to orient the 1D pattern along the desired compression angle [with respect to the y axis in Fig. 1(a)] and cropped in a rectangular shape, to achieve a homogeneous secondary

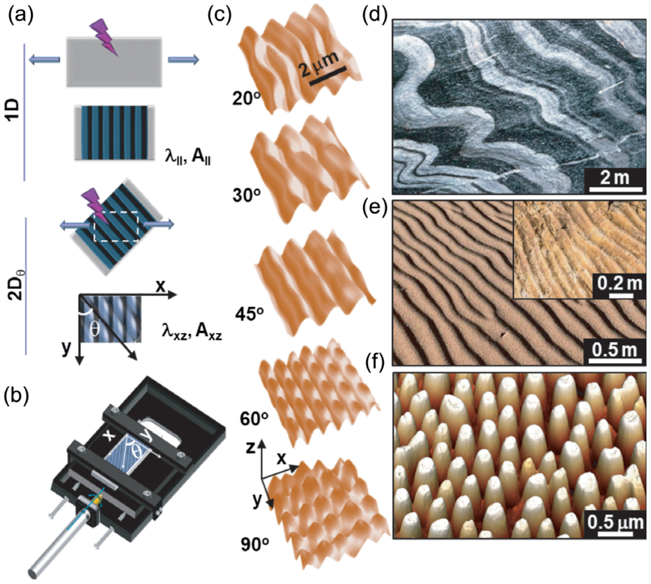

FIG. 1. (a) Fabrication of wave ripples on elastomeric surfaces by sequential biaxial wrinkling at compression angle θ between generations. (b) Linear strain stage and second generation. (c) AFM scans of surfaces at varying θ, exhibiting a transversal (xy) instability, reminiscent of wave ripples. Multiscale images of (d) layered rock planes folded under directional, sequential stress (courtesy of D. Chew, Trinity College Dublin); (e) sand ripples formed by wind action, and (inset) fossilized bedform in Dinosaur Ridge, CO; and (f) nanoscale patterns on cicada wings (specimen courtesy of B. Price, Natural History Museum, London).

strain field during the plasma oxidation step. Once strain is released, a $2D_{\theta}$ pattern is formed, resulting in second generation features defined as λ_{xz} and A_{xz}. A plethora of new patterns are obtained, illustrated in Fig. 1(c), distinct from those formed via simultaneous bi- or multiaxial wrinkling, noticeably due to the transverse instability developing in the xy plane, with counterparts in varied naturally occurring patterns of distinct origin [Figs. 1(d)–1(f)].

Figure 2 examines the surface patterns formed by symmetric plasma exposure ($\tau_1 = \tau_2 = 120$ s) and prestrain $\epsilon_1 = \epsilon_2 = 10\%$, and variable θ, such that both wrinkling generations involve the same skin thickness h, and thus potentially the same λ and A; these are mapped by optical and atomic force microscopy (AFM, Bruker Innova, Al-coated SiN_4 tips), and small angle light scattering (SALS, 533 nm, 500 mW diode Crystalaser).

When both generations have the same orientation ($\theta = 0°$) uniaxial sinusoidal wrinkling is observed, while orthogonal generations ($\theta = 90°$) give rise to a "symmetric checkerboard" topography [26–28]. At intermediate angles, the wave interference between generations in the xy plane results in a coupled transverse oscillation, locked into patterns termed "ripples." Fourier-space analysis by SALS characterizes the wave number and orientation of the diffraction orders, and thus the real space periodicity and actual orientation, θ_{exp}, of the resulting surface waves.

A nonmonotonic variation in λ_{xz} with θ is readily observed; increasing up to 30° and then decreasing at 50°, towards the checkerboard morphology. This is interpreted in terms of a destabilization of the original surface profile under strain, that induces a localized buckling event in the direction of the applied strain. The rearrangement initiates from pattern defects, including dislocations, and propagates to neighboring waves by the growth of domains with in-plane "kinks" or "bends." The resulting localized transition zones are reminiscent of the hierarchical patterns formed in thin sheets under boundary confinement [29]. This transverse buckling instability in the xy plane, and formation of diagonal sinuous patterns, depends on the imposed compression angle θ between generations, illustrated as blue and cyan lines in the schematics of Fig. 2(c); black circles indicate bends, defining the pivot of the different directions of the xy plane sinusoids. Significantly, their linear number density increases with θ, but the pivot angle ϕ appears to be *constant* under these conditions. Above a threshold compression θ ($\gtrsim 15°$), the localized instability propagates spatially across the surface, as detailed in Figs. S1 and S2 [30]. These patterns are reminiscent layered metamorphic sinuous belts formed under progressive shear [9,31,32].

A minimal mathematical description of these surface topographies is tentatively expressed in terms of a summation of sinusoidal waves [33], arranged at a prescribed relative θ, parameterized by the wrinkling behavior of a bilayer under uniaxial compression [34–36]:

$$w(x, y) = A_1 \cos(k_1 x_1) + A_2 \cos(k_2 x_2), \tag{1}$$

where the x_2 coordinate axis, corresponding to the second generation, is defined along the x axis (thus $x_2 \equiv x$), and x_1 is oriented with respect to the x axis by (compression) angle θ, such that $x_1 = x\cos(\theta) + y\sin(\theta)$. Since the prestrain $\epsilon = 10\% \lesssim 20\%$, amplitudes A_i and wave numbers k_i of each generation might be expected to follow the low deformation buckling limit [37]:

$$A_i = h_i \left(\frac{\epsilon_i}{\epsilon_c} - 1\right)^{\frac{1}{2}}, \tag{2}$$

and wave number $k_i = 2\pi/\lambda_i$, where

$$\lambda_i = 2\pi h_i \left(\frac{\bar{E}_f}{3\bar{E}_s}\right)^{\frac{1}{3}}, \tag{3}$$

h_i is the thickness of the glassy skin, $\bar{E}_f$ and $\bar{E}_s$ are the plane strain modulus of the film and the substrate, respectively, and $i = 1, 2$ denotes each generation; the critical strain, which must be exceeded to trigger the instability $\epsilon_c = 1/4(3\bar{E}_s/\bar{E}_f)^{2/3} \simeq 2.5\%$ in our experiments. The surface topography Eq. (1) is thus expressed in terms of the principal coordinates x and y as

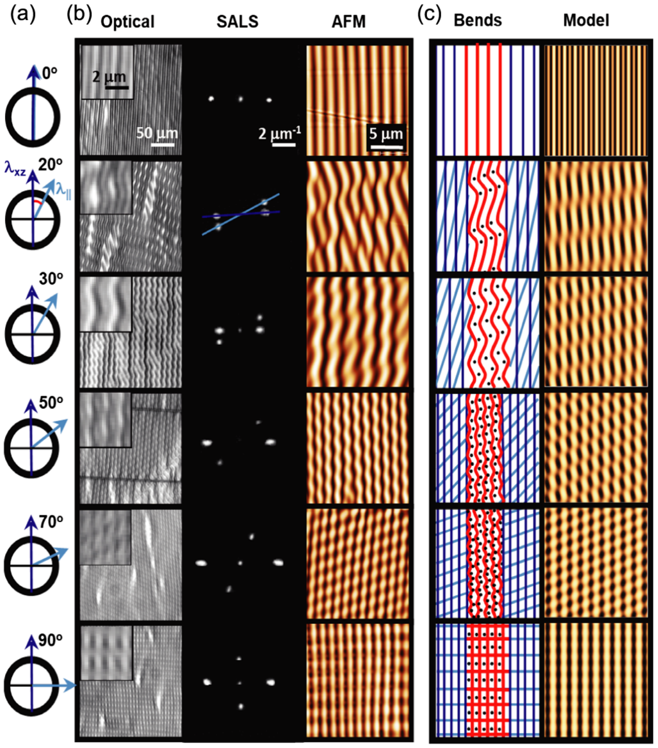

FIG. 2. (a) Compression angle θ, defined between the first (cyan) and second (blue, vertical) generations, with respective wavelengths $\lambda_{\parallel}$ and λ_{xz}. (b) Corresponding wrinkling topographies examined by optical microscopy, SALS and AFM. (c) Skeletal diagram of the interference pattern (red) and bending points on the xy plane whose number density depends on θ; model computed from Eq. (5).

$$w(x,y) = A_1 \cos[k_1 \cos(\theta x)] \cos[k_1 \sin(\theta y)] - A_1 \sin[k_1 \cos(\theta x)] \sin[k_1 \sin(\theta y)] + A_2 \cos(k_2 x) \tag{4}$$

accounting for the diagonal superposition of the two wrinkling waves. As both generations in the experiments reported in Fig. 2 are nominally identical, Eq. (4) would simplify by $A_1 = A_2 \equiv A$ and $k_1 = k_2 \equiv k$, whose result is shown in Fig. 2(c). Despite its simplicity, the model qualitatively captures the experimental data well, yet quantitative variations are found, discussed next.

Figure 3(a) illustrates a detailed surface profile, depicting the transverse xy periodic undulations caused by the interference of the two generations, propagating from a local event, or defect, upon strain relaxation accompanying the emergence of the second wrinkling generation (Fig. S2). The first generation is oriented at the prescribed θ with respect to the vertical blue dashed line representing the second generation (dashed) line. The presence of the underlying first generation, deforms the second generation fold line from a straight trajectory into a “ripple” sinuous front (purple) line. In the process, a new characteristic wavelength in the xy plane emerges, defined as the distance between two maxima or λ_{xy}. Concurrently, the superposition produces a sinusoidal profile in the xz plane defined by a λ_{xz}, corresponding to where the second generation would be expected.

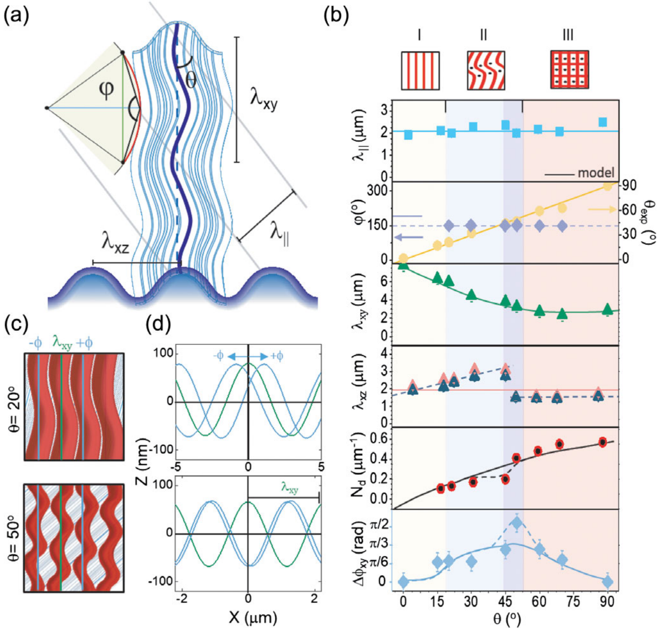

FIG. 3. (a) Schematic of transverse wave ripples with first generation (gray, $\lambda_{\parallel}$), oriented at angle θ with respect to second generation (dashed line, λ_{xz}). Undulations along the ripple (purple) define additional periodicity λ_{xy} on the xy plane, and bending angle ψ (violet), (b) angle dependence of: first generation $\lambda_{\parallel}$; bending angle ψ and measured compression θ_{exp}; in-plane undulation λ_{xy}; second generation λ_{xz} (pink: AFM; blue: SALS); linear number density N_d of bends (“defects”); phase difference $\Delta\phi$. Solid lines indicate our minimal model, with deviations shown as dashed lines (see text). Three regimes are termed: I “constrained 1D folds,” II “ripples” form, and III “checkerboard.” (c) $\Delta\phi$ illustrated for $\theta = 20°$ and 50°, approximately in and out of phase. (d) Corresponding AFM profiles along representative vertical traces in (c), and phase angle $\pm\phi$.

The overall surface characteristics are summarized in Fig. 3(b), as a function of the imposed compression θ. We find that $\lambda_{\parallel}$ remains constant within experimental uncertainty (Fig. S4), and its value ($\simeq 2.1$ μm) agrees with that expected from Eq. (3), implying that the second generation wrinkling has minimal impact on the periodicity of the first generation. The measured compression angle θ_{exp} by SALS agrees (within uncertainty of $\pm 3°$) with the imposed θ. Significantly, we find that the transverse xy ripple pattern exhibits a *constant* bending angle $\psi \simeq 150°$ (violet), for all imposed θ between the two generations. The emerging transverse λ_{xy} decreases steadily with θ and is well predicted by the minimal model (solid line). Unlike the first generation wavelength, the second generation λ_{xz} deviates nonmonotonically from the uniaxial prediction, Eq. (3), for the wrinkling of a planar bilayer, in order to accommodate the interaction between neighboring ripples.

The defect linear number density N_d, computed from the observed bends (or kinks) in the xy instability, approximately follows the number of intersections between the maxima of the two generations (solid line). Pattern inspection reveals that the transverse instability emanates from defects that accommodate the incommensurate length scales defined by the straightforward wave summation and the emerging constant constant bending seven angle ψ of 150°. This frustration results in a defect front propagation in the transverse plane, transferring strain to neighboring ripples [38], altering the periodicity, in a manner that depends on the orientation of the strain components. As the bending rigidity of the corrugated film surface becomes anisotropic [27], this change in effective skin modulus likely impacts λ_{xz}, at otherwise constant conditions.

The effect in λ_{xz}, shown by SALS and AFM is translated in an increase at low θ, until 45°, which then abruptly decreases from 50°, remaining constant up to 90°. This discontinuity is mirrored in N_d and in the phase difference $\Delta\phi$ between adjacent ripples, illustrated in Fig. 3(c). Tracing vertical profile lines in the xy plane along the curved fold line of the wave ripples, the profile and phases ($-\phi$ and $+\phi$) of neighboring undulations were computed from the AFM profiles along the x direction, shown in Fig. 3(d) (depicted for $\theta = 30°$ and 50°). From 0°, $\Delta\phi$ initially increases, until an out-of-phase configuration is locked at $\theta \simeq 50°$. At low θ ($0° < \theta < 10°$), the phase shift remains zero, meaning that a constrained regime of 1D wrinkling interference is preferred and no λ_{xy} is observed, labeled as regime I. When $\theta \geq 15°$, the torsion induced by the first generation triggers the formation of ripples, with phase shift $\Delta\phi \simeq \pi/6$. Up to $\theta = 45°$, in regime II, twisted wrinkles dominate, accompanied by shorter λ_{xy}, and a gradual deviation of λ_{xz} away from its one-dimensional value, up to 3.5 μm at 45°.

Around $\theta = 50°$, N_d increases rapidly, and the pattern reaches an out-of-phase configuration with phase shift $\Delta\phi \simeq \pi/2$. Further increasing θ induces a transition towards checkerboards, in regime III, as the bend density N_d suffices to reach a new energetically favorable pattern; here $\Delta\phi$ progressively decreases, vanishing at $\theta = 90°$, and λ_{xy} decreases to its undisturbed one-dimensional value. The reduction in λ_{xz} below its equilibrium value of 2.1 μm can be rationalized due to the compression in the first generation pattern (approximately 10%) as the second generation is excited, leading to a slight shortening in periodicity. Analogous behavior is observed in the evolution of the pattern amplitude (Fig. S3), and further discussion of experimental deviation from the minimal wave superposition model is presented in Fig. S5.

In order to examine the significance of the constant bending angle ψ, a series of experiments probing the effect of skin thickness was performed by varying plasma exposure time $\tau = \tau_1 = \tau_2$ from 30 to 300 s, at fixed compression angle $\theta = 20°$, coinciding with regime II where ripple patterns are formed. The results are reported in Fig. 4. The glassy skin thickness h increases logarithmically with τ [22] causing the transverse buckling instability to evolve towards straight folds at 300 s [and trivially increase λ and A from Eqs. (2)–(3)].

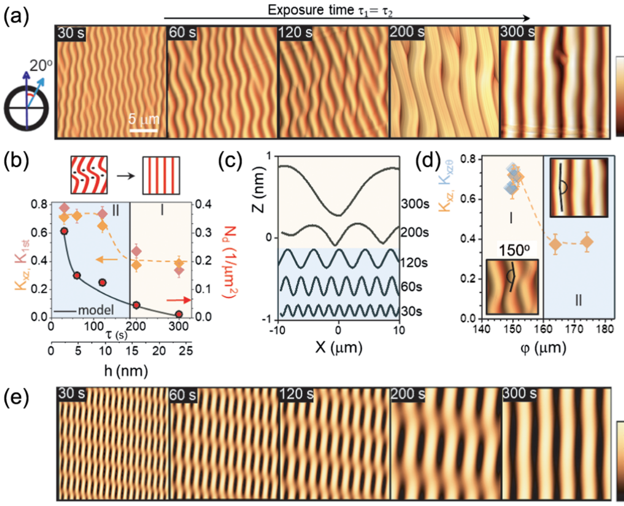

FIG. 4. (a) AFM scans of wave ripple patterns with increasing skin thickness (via plasma exposure time $\tau_1 = \tau_2$), at constant $\theta = 20°$. (b) Dependence of pattern curvature of the first ($K_{\parallel}$) and second (K_{xz}) generation pattern and defect linear number density, N_d, on skin thickness h, showing a return from ripples (regime II) to 1D wrinkling (regime I). (c) AFM profiles of the surfaces in (a) as increasing plasma exposure time (from bottom to top). (d) Decrease in K_{xz} with in-plane bending angle ψ; also shown $K_{xz\theta}$ (blue) computed from Fig. 2. (e) Model profiles corresponding to conditions in (a), computed from Eq. (4).

The xy interference is characterized by measuring the bending angle ψ from the AFM images and from the first generation curvature angle data (Fig. S6). Figure 4(b) shows the dependence of the xz curvature, K_{xz}, and the first generation curvature $K_{1\mathrm{st}}$ with exposure time and skin thickness h. They remain approximately constant up to $h \simeq 15$ nm, and then drop to a lower value. As expected N_d also drops, beyond the trivial scale increase of pattern dimensions. The 30 s pattern, corresponding to the thinner glassy skin, is the most regular, associated with its ability to accommodate and propagate defects. As the surface curvature decreases, surface undulations progressively flatten and broaden [Fig. 4(c)], impeding interference between generations and reverting the regime II to I, accompanied by an increase of the bending angle ψ. Figure 4(d) establishes the relationship between the curvature of $K_{xz\theta}$ (obtained from Fig. 2) and K_{xz} (from the time series) with the bend angle ψ, corroborating this angle depends on the skin thickness alone (and not on θ) via the overall pattern curvature. Progressive skin thickening reduces the defect propagation due to the increase of bending stresses and therefore limiting and increasing the critical strain for the secondary buckling excitation, which leads to the loss of the kink defects and preferential formation of "constrained 1D" patterns [39]. The minimal model [Fig. 4(e)] at constant θ qualitatively captures the straightening of the ripple pattern and effective ψ.

This sequential wrinkling approach provides a facile and scalable framework to induce tunable undulated and checkerboard patterns, by varying layer skin and strain parameters. Our findings hold for other bilayer geometries, such as polymer laminates fabricated by thin film floating (Fig. S7). Here, only symmetric variations in skin thickness (via τ) and strain ϵ of both generations were considered, suggesting that numerous other patterns, and nested patterns, are attainable. Their scale can also be tuned by several orders of magnitude via different skin formation approaches, for instance beyond 100s of μm by UV ozonolysis [21,26]. Despite its limitations, the minimal model assuming the summation of waves, with λ and A adequately parameterized by experiment, can guide surface fabrication, mimicking naturally occurring patterns, with potential practical application.

We acknowledge the HORIZON 2020 EU Framework Programme (MSCA-ITN-722871-BIOCLEAN), EPSRC (CDT Plastic Electronics), Procter & Gamble and the Royal Academy of Engineering (UK) for funding. We thank David Chew, Trinity College Dublin, for the photograph in Fig. 1(d), Ben Price, Natural History Museum, London, for the cicada specimen imaged in Fig. 1(f), and Jack F. Douglas, NIST, for useful discussions.

---

[*] j.cabral@imperial.ac.uk

[1] R. S. Anderson, Earth-Sci. Rev. **29**, 77 (1990).

[2] C. R. Thorne, R. C. MacArthur, and J. B. Bradley, *Physics of Sediment Transport by Wind and Water: A Collection of Hallmark Papers by R.A. Bagnold* (American Society of Civil Engineers, New York, 1988).

[3] J. L. Hansen, M. van Hecke, A. Haaning, C. Ellegaard, K. H. Andersen, T. Bohr, and T. Sams, Nature (London) **410**, 324 (2001).

[4] V. Langlois and A. Valance, Phys. Rev. Lett. **94**, 248001 (2005).

[5] P. Coullet and J. Lega, Europhys. Lett. **7**, 511 (1988).

[6] T. B. Benjamin, Proc. R. Soc. A **328**, 153 (1972).

[7] T. B. Benjamin and J. Feir, J. Fluid Mech. **27**, 417 (1967).

[8] M. Fermigier, L. Limat, J. Wesfreid, P. Boudinet, and C. Quilliet, J. Fluid Mech. **236**, 349 (1992).

[9] J. G. Ramsay, J. Geol. **70**, 309 (1962).

[10] H. Ramberg, Tectonophysics **1**, 307 (1964).

[11] S. K. Ghosh, Tectonophysics **9**, 559 (1970).

[12] A. Gierer and H. Meinhardt, Kybernetik **12**, 30 (1972).

[13] E. P. Ivanova, J. Hasan, H. K. Webb, V. K. Truong, G. S. Watson, J. A. Watson, V. A. Baulin, S. Pogodin, J. Y. Wang, M. J. Tobin *et al.*, Small **8**, 2489 (2012).

[14] N. Bowden, S. Brittain, A. G. Evans, J. W. Hutchinson, and G. M. Whitesides, Nature (London) **393**, 146 (1998).

[15] J. Genzer and J. Groenewold, Soft Matter **2**, 310 (2006).

[16] J. Allen, Sedimentology **2**, 93 (1963).

[17] C. M. Stafford, C. Harrison, K. L. Beers, A. Karim, E. J. Amis, M. R. VanLandingham, H.-C. Kim, W. Volksen, R. D. Miller, and E. E. Simonyi, Nat. Mater. **3**, 545 (2004).

[18] N. Bowden, W. T. Huck, K. E. Paul, and G. M. Whitesides, Appl. Phys. Lett. **75**, 2557 (1999).

[19] D. Breidand A. J. Crosby, Soft Matter **5**, 425 (2009).

[20] M. Watanabe, Polym. Adv. Technol. **16**, 744 (2005).

[21] K. Efimenko, M. Rackaitis, E. Manias, A. Vaziri, L. Mahadevan, and J. Genzer, Nat. Mater. **4**, 293 (2005).

[22] F. A. Bayley, J. L. Liao, P. N. Stavrinou, A. Chiche, and J. T. Cabral, Soft Matter **10**, 1155 (2014).

[23] M. Nania, F. Foglia, O. K. Matar, and J. T. Cabral, Nanoscale **9**, 2030 (2017).

[24] S. Cai, D. Breid, A. J. Crosby, Z. Suo, and J. W. Hutchinson, J. Mech. Phys. Solids **59**, 1094 (2011).

[25] X. Chen and J. W. Hutchinson, J. Appl. Mech. **71**, 597 (2004).

[26] A. Chiche, C. M. Stafford, and J. T. Cabral, Soft Matter **4**, 2360 (2008).

[27] C. S. Davis and A. J. Crosby, J. Polym. Sci., Part B **50**, 1225 (2012).

[28] L. Pellegrino, S. Khodaparast, and J. T. Cabral, Soft Matter **16**, 595 (2020).

[29] H. Vandeparre, M. Piñeirua, F. Brau, B. Roman, J. Bico, C. Gay, W. Bao, C. N. Lau, P. M. Reis, and P. Damman, Phys. Rev. Lett. **106**, 224301 (2011).

[30] See Supplemental Material at http://link.aps.org/supplemental/10.1103/PhysRevLett.128.058001 for details of sample preparation and characterization; onset angle θ for ripple formation; defect propagation upon strain release; strain component decomposition; statistical variation in $\lambda_{\parallel}$; further detail on model comparison; estimation of bending angle; ripples via polymer film floating and lamination.

[31] S. Sengupta, S. Ghosh, S. Deb, and D. Khan, J. Struct. Geol. **27**, 1282 (2005).

[32] J. Carreras, E. Druguet, and A. Griera, J. Struct. Geol. **27**, 1229 (2005).

[33] R. C. Fletcher, J. Struct. Geol. **13**, 87 (1991).

[34] A. Volynskii, S. Bazhenov, O. Lebedeva, and N. Bakeev, J. Mater. Sci. **35**, 547 (2000).

[35] R. Huang and Z. Suo, J. Appl. Phys. **91**, 1135 (2002).

[36] G. Gough, C. Elam, G. Tipper, and N. De Bruyne, Aeronaut. J. **44**, 12 (1940).

[37] H. Jiang, D.-Y. Khang, J. Song, Y. Sun, Y. Huang, and J. A. Rogers, Proc. Natl. Acad. Sci. U.S.A. **104**, 15607 (2007).

[38] T. Ohzono and M. Shimomura, Langmuir **21**, 7230 (2005).

[39] B. Roman and A. Pocheau, J. Mech. Phys. Solids **50**, 2379 (2002).